

Fluctuations of local plastic strain in granular media

I. Awada, M. Bornert, V. Langlois, J. Léopoldès*

Navier, Univ. Gustave Eiffel, École des Ponts, CNRS, F-77454 Marne-la-Vallée, France

(Dated: March 24, 2025)

We experimentally study the heterogeneity of strain in a granular medium subjected to oscillatory shear in a rotating drum. Two complementary methods are used. The first method relies on optical imaging and grain tracking, allowing us to compute some components of the strain tensor and their variance. The second method, Diffusive Acoustic Wave Spectroscopy (DAWS), provides the variance of strain components within the bulk. Our results show that strain is spatially heterogeneous, with fluctuations about ten times larger than the mean, primarily dominated by variability at the grain scale. We then analyze in detail the strain fluctuations occurring during the forward and backward branches of the shear cycles, as well as the plastic strain at the completion of each cycle. Both methods reveal that each shear cycle consists of two consecutive diffusive-like branches, and that the resulting plastic strain fluctuations grow linearly with shear. We propose a simple framework to rationalize these effects, suggesting that plastic strain fluctuations increase with the diffusion coefficient and decrease with the anticorrelation between forward and backward strain, which is enhanced in denser packings.

I. INTRODUCTION

Solids respond elastically to shear at low strain, then progressively yield and eventually fail. In heterogeneous and discrete solid systems composed of particles, such as foams, emulsions, colloidal glasses, or granular media, macroscopic plasticity develops through complex mechanisms at the scale of one to ten particle diameters. For example, rearrangements in foams and emulsions are known as T1 events (neighbor switching between four particles) [1, 2]. In colloidal glasses, Eshelby-like inclusions are responsible for plastic strain [3]. In granular media, strain is highly non-affine, as evidenced by the emergence of vortex-like structures [4, 5] and the presence of defects similar to T1 events [6]. Still, how the intensity of plastic strain fluctuations depends on system packing density and applied strain/stress remains poorly understood in three-dimensional systems.

In this context, it is essential to develop experimental methods capable of resolving particle rearrangements in granular media. Bulk particle rearrangements can be investigated using scanning techniques such as laser sheet imaging [7], confocal microscopy [3], or X-ray tomography [8]. Additionally, diffusing wave spectroscopy (DWS) is a well-established method for studying divided matter, providing estimates of the random relative displacement between particles such as drops, colloids, or bubbles [9–11]. In granular materials, diffusive light scattering has been extensively used to probe interactions between strain heterogeneities at the scale of about 10 grain diameters [12, 13] and to analyze velocity fluctuations in the liquid state [14]. Since the wavelength of ultrasound can be easily adjusted to match the size of a grain, Diffusive Acoustic Wave Spectroscopy (DAWS) enables the measurement of kinematics at the grain scale [15], revealing the transition from reversible to irreversible local grain motions at the macroscopic flow threshold [16]. However, applying DAWS to sheared granular media has not yet enabled a quantitative analysis of strain fluctuations.

This paper has two main objectives. First, it proposes a method for monitoring strain fluctuations at the grain scale in sheared granular media. Second, it offers new insights into the dependence of the intensity of local strain heterogeneity on macroscopic shear.

II. EXPERIMENTS

The system consists of a dense granular material immersed in water and subjected to oscillatory rotational motion. This setup is relevant to soil creep [17], with its associated natural hazards, as well as to diffusion-induced granular mixing [18]. The granular material is placed inside a rotating drum that oscillates slowly at angles lower than the angle of repose. Given the quasi-static loading, the liquid water does not influence grain rearrangement.

Two series of experiments were conducted using the same preparation protocol but different measurement techniques. The first method involves analyzing the two-dimensional kinematics by tracking the positions of grains located

* julien.leopoldes@univ-eiffel.fr

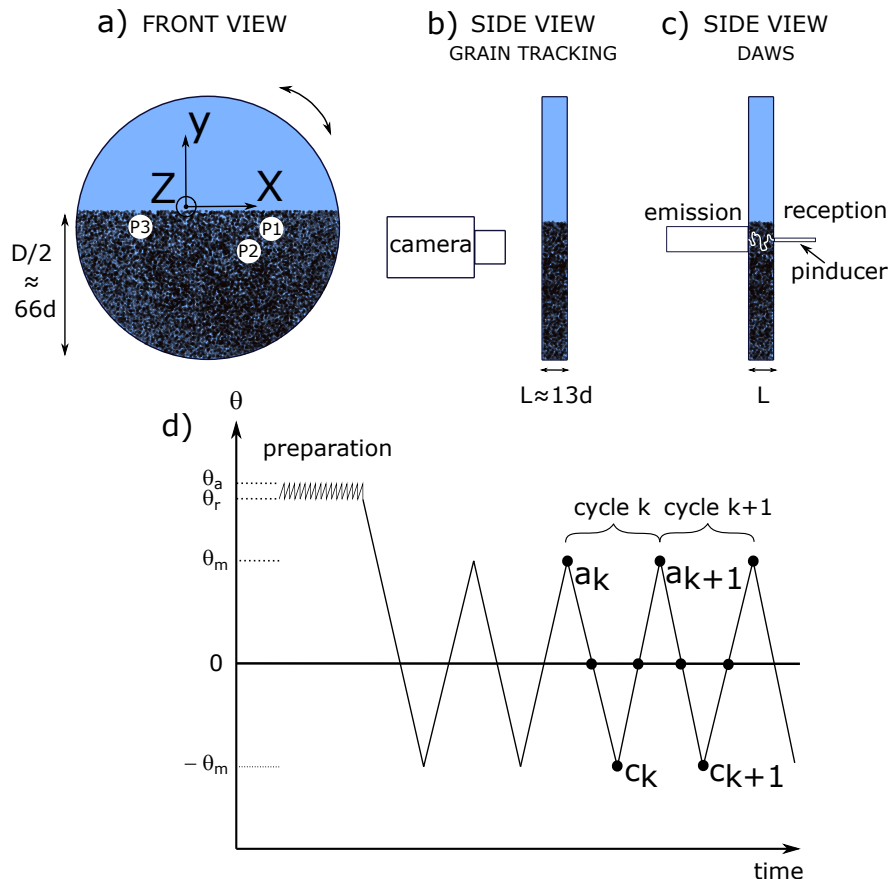


FIG. 1. Sketch of the experiment. The rotating drum (radius $D/2 = 100$ mm and thickness $L = 20$ mm) is filled with grains and water. (a) The front view shows the grains and the three zones of interest analyzed. (b) The side view for the grain tracking method shows the camera, which rotates with the drum. Only the grains at the front face are imaged. (c) The side view for the DAWS setup illustrates the ultrasound emission and reception transducers. The thick white line represents an arbitrary diffusive path. (d) For both the grain tracking method and DAWS, the preparation protocol begins with the continuous rotation of the drum, producing several consecutive avalanches. Then, the free surface is brought to an angle $+\theta_m$, lower than the angle of repose, and subjected to 50 oscillations between $+\theta_m$ and $-\theta_m$. Black points indicate the angles at which images or ultrasonic signals are recorded. The notations a_k and c_k are introduced later in the text to define the pairs of images (two granular configurations) between which the strain is analyzed.

at the front face of the drum. The second method, DAWS, is a three-dimensional probe of the granular medium and relies on the correlation of ultrasound signals propagating through the water pores.

A. Preparation protocol of the initial state

A sketch of the rotating drum is provided in Figure 1 a), b), and c). After introducing the grains (ceramic, diameter $d = 1.50 \pm 0.08$ mm), the drum is mounted on a rotating stage. It is then filled with water, ensuring the removal of any air bubbles. Each experiment is preceded by a rapid, continuous clockwise rotation of the drum by at least 180° . The preparation protocol then consists of a quasi-static anticlockwise rotation, inducing approximately twenty consecutive avalanches (Figure 1 d)). This quasi-static rotation allows us to measure two characteristic angles, defined as the inclination θ of the granular free surface relative to the horizontal plane. The avalanche angle, $\theta_a = 25.5^\circ$, represents the maximum inclination before an avalanche occurs, while $\theta_r = 22.8^\circ$ is the inclination at which the granular medium stops flowing [19]. Consequently, the preparation protocol ensures that the free surface of the granular medium is initially inclined at $\theta \approx \theta_r$. At this stage, the drum is rotated so that the free surface is set to an inclination $\theta_m < \theta_r$ (Fig. 1d)). The system is then subjected to 50 oscillations at $\theta = \pm\theta_m$, indexed by $1 \leq k \leq 50$. We present results for four different values of θ_m : 21.8° , 19.8° , 16.8° , and 10.8° . For ensemble averaging, the entire preparation protocol and the subsequent fifty shear cycles are repeated 10 times for each θ_m .

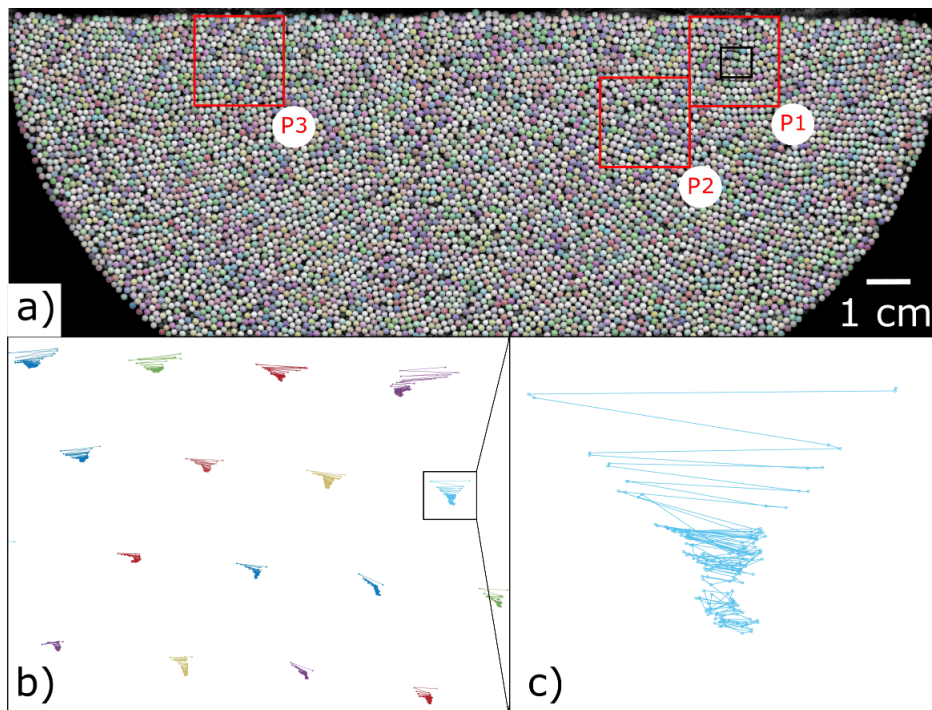


FIG. 2. Typical image taken at the front face of the drum, illustrating examples of grain detection and tracking. a) Each detected grain is arbitrarily colored. The positions "P1", "P2", and "P3", outlined by red squares, correspond to the zones of interest where deformation is computed and compared with the decorrelation of acoustic signals. b) Reconstructed trajectories over 50 oscillations at position P1, located within the black square in (a). c) Zoom on a selected trajectory from (b).

B. Image analysis

The granular medium is characterized by capturing four images per cycle of the grains at the front face of the drum using the camera, as indicated by the black dots in Figure 1d). An example of such an image is shown in Figure 2a). We present data for three different areas of interest, fixed on the side of the drum. Two of these areas are near the free surface (P1 and P3), while the third one is located deeper within the packing (P2), as shown in Figure 2a).

1. Grain detection and tracking

For each image, we apply a deep learning method to detect the grains and segment the image [20]. To train the model, we performed a meticulous manual annotation of grain contours on a series of images. From the segmentation results, the center of each grain was determined as the weighted average position of the pixels in the detected region, with weights given by the gray levels. Subsequently, a tracking algorithm [21] was used to reconstruct grain trajectories during the drum oscillations. A selection of the reconstructed trajectories is shown in Figure 2 b) and c). The grains oscillate as they gradually sink under the effect of gravity.

During the initial oscillations, grain motion can be significant ($> d/2$), leading to inaccurate tracking. To ensure robust analysis, we retain only images where grain tracking can be visually validated. The first cycle in which grains are accurately tracked is $k_r = 4, 3, 2, 1$ for $\theta_m = 21.8^\circ, 19.8^\circ, 16.8^\circ$, and 10.8° , respectively. This first cycle is marked with a star in Figure 3a).

2. Strain analysis and averaging procedure

The set of grain coordinates is used to construct a Delaunay triangulation, where the triangle vertices correspond to the centers of mass of the grains. The various components of the strain (symmetric part of the strain tensor) are then computed at the grain scale following Bagi [22]. Throughout this paper, these triangles will be referred to as "Bagi cells" (strain noise level 10^{-4}). An example of such Bagi cells, color-coded according to the strain magnitude, is

shown in Figure 5a). We have verified (not shown) that the average volumetric strain, weighted by area and computed over the entire drum, matches the volumetric strain derived from the displacement of the granular free surface.

The 2D strain in Bagi cells is averaged over bins (zones $P1$, $P2$, $P3$) of size $13 d \times 13 d$, as shown by the red squares in Figure 2a). This spatial average is denoted by $\bar{\cdot}$. The size of these zones is chosen to match the surface area illuminated by ultrasound waves in the DAWS method (see Appendix A). Other averaging zone sizes will be used occasionally and will be explicitly mentioned.

Because the Bagi cell strain measurements are obtained from experiments different from those using DAWS (as the acoustic sensors obstruct the field of view), comparing the results from both methods also requires ensemble averaging. This ensemble averaging is performed over 10 experiments, and the resulting strains are denoted as $\langle \bar{\cdot} \rangle$. Additionally, some correlations between individual Bagi cells will be computed without averaging.

The optical imaging method allows us to compute the strain components $\langle \overline{\epsilon_{xx}} \rangle$, $\langle \overline{\epsilon_{yy}} \rangle$, $\langle \overline{\epsilon_{xy}} \rangle$, and $\langle \overline{\epsilon_v} \rangle$, while $\langle \overline{\epsilon_{zz}} \rangle = 0$ due to the presence of solid walls. In addition to being limited to two dimensions, optical imaging captures the kinematics of grains at the front face of the drum, which may behave differently from those within the bulk. For instance, it is well known that in flowing granular media, solid walls induce layering, density oscillations, and inhomogeneous granular temperature [23].

The strain is computed from a pair of granular configurations p_1 and p_2 selected from the set $\{a_k, c_k\}$ with $k_r \leq k$. This pair is denoted as $[p_1, p_2]$, where p_1 serves as the reference configuration.

3. Free surface

A useful analysis is the detection of the free surface to estimate the variation in the global solid fraction throughout the experiments. We first divide the image into 30 vertical stripes of equal width (4d). Then, we compute the profile of intensity for each stripe and apply a detection threshold to find the position of the free surface y_s for each stripe. We calculate its average position throughout the width of the drum $\overline{y_s}$ followed by ensemble averaging. The vertical displacement of the free surface from its initial position that was reached at the end of the protocol of preparation is defined as $\langle \overline{-s_y} \rangle = \langle \overline{y_s(k)} \rangle - \langle \overline{y_s(0)} \rangle$. Unlike grain tracking, free surface detection can be performed as early as the first oscillation cycle. For comparison, the first cycles from which grain tracking could be performed are annotated by stars in Figure 3 a).

C. Diffusing acoustic wave spectroscopy

It is also desirable to probe the granular medium in the bulk, which is achieved using DAWS. When the wavelength of a propagating wave is on the order of the particle size, multiple scattering occurs due to the numerous scatterers encountered along the wave's path. DAWS relies on analyzing the variations in the phase variance of the propagating signal along the acoustic path of n scatterers (grains), caused by their relative motion [15, 24].

However, in sheared granular media, interpreting the decorrelation of multiply scattered waves is complex due to strain heterogeneities across multiple length scales (grain scale, shear bands). Additionally, ubiquitous phenomena such as compaction and plasticity make ensemble averaging challenging. Below, we propose a protocol to extract meaningful kinematic information from DAWS in dense granular media, allowing for comparison with the previous method based on direct grain tracking.

The scattered waves produce signals, Ψ_i and Ψ_j , measured for two slightly different granular configurations, which are compared by computing a correlation function g_1 :

$$g_1 = \frac{\int \Psi_i \Psi_j dt}{(\int \Psi_i^2 dt \int \Psi_j^2 dt)^{1/2}} \quad (1)$$

g_1 represents the spatial average of the many scattering events occurring within the volume probed by the wave. When ultrasound is used to monitor structural changes in the granular packing under oscillations, the decorrelation of the signals reflects relative grain displacements, or strains, at the length scale of the mean free path $l \sim \lambda \sim d$ [15], see Appendix A.

The works of Bicout et al. [25] and Cowan et al. [15] establish the relationship between the ensemble-averaged g_1 and the phase shift of a single scattering event, $\Delta\Phi$, induced by local strains:

$$g_1 = \cos(n\langle\Delta\Phi\rangle) \times \exp\left(-\frac{n}{2}V(\Delta\Phi)\right). \quad (2)$$

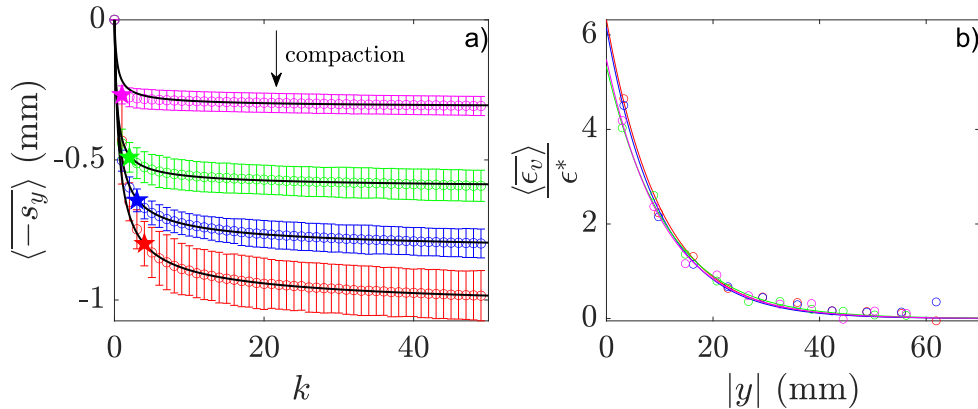


FIG. 3. a) Variation of the free surface position as a function of the number of oscillations. The curves, from lowest to highest, correspond to $\theta_m = 21.8^\circ$, 19.8° , 16.8° , and 10.8° . The black lines represent the fit from the model proposed by [26]. The fitted parameters are provided in the appendix (see Fig. 10). A star denotes the first images where grain tracking could be performed. b) Profile of the volumetric strain $[a_{k_v}, a_{50}]$ along the vertical axis $\langle \epsilon_v(\theta_m) \rangle$, normalized by the mean value ϵ^* over the region $0 < |y| < 60$ mm. The colors red, blue, green, and pink correspond to $\theta_m = 21.8^\circ$, 19.8° , 16.8° , and 10.8° , respectively. Experimental data are represented by circles, while the thin lines represent the exponential fit (as described in the text).

where $\langle \Delta\Phi \rangle$ is the average phase shift, $V(\Delta\Phi)$ the variance and n the number of scattering events along the acoustic path. In addition, the authors show that :

$$\langle \Delta\Phi \rangle = \frac{1}{3}ql\langle \epsilon_v \rangle, \quad (3)$$

$$V(\Delta\Phi) = \frac{2}{15}(ql)^2 \left(\langle \epsilon_v^2 \rangle + 2 \times \sum_{i,j} \langle \epsilon_{i,j}^2 \rangle \right), \quad (4)$$

where $q = 2\pi/\lambda$ and l is the mean free path. Hence, with $\langle \epsilon_v \rangle$ and g_1 we can determine the phase variance $V(\Delta\Phi)$ using Eqs. 2 and 3. This, in turn, allows us to compute the sum of quadratic terms on the right-hand side of Eq. 4, denoted as $\langle \epsilon^2 \rangle_u$.

In a specific set of experiments that solely involve acoustic measurements, we use the rotating drum equipped with a pair of ultrasound emitter-receiver transducers, as illustrated in Figure 1 c). In this configuration, grain tracking is not possible because the transducers obstruct the field of view. Briefly, a pulse is emitted by a 1 MHz immersion transducer (diameter $d_t = 13$ mm, Panametrics) and received by a small pinducer with a diameter of $d_p = 1.5$ mm. Given the corresponding wavelength $\lambda = 1.5$ mm, which is approximately equal to d_p , the waves undergo multiple scattering [15, 24]. In the present study, DAWS probes the medium at the length scale of the grains, sampling a volume roughly corresponding to $d_t^2 \times L \sim 10^3 d^3$. More details about DAWS are provided in Appendix A.

III. RESULTS

A. Compaction

As the number of oscillations increases, the granular material undergoes compaction, as evidenced by the variation of $\langle -s_y \rangle$ shown in Figure 3 a). Higher oscillation angles result in denser packings for a fixed number of oscillations. Additionally, compaction occurs more rapidly at larger oscillation angles. The evolution of packing fraction during shaking is fitted to the standard logarithmic law, as proposed by [26], and is presented in Figure 3 a). The equation used for the fitting and the corresponding parameters are provided in Appendix B, Figure 10. It can be observed that the quasi-static oscillations employed in this study have a similar effect to vertical mechanical taps [26] in terms of compacting the granular material.

Furthermore, as reported in [26], the compaction is spatially heterogeneous, being more pronounced near the free surface than in the bulk of the granular medium. To capture this spatial variation with sufficient resolution, we apply a specific binning technique along the vertical direction by dividing the drum images into horizontal stripes of

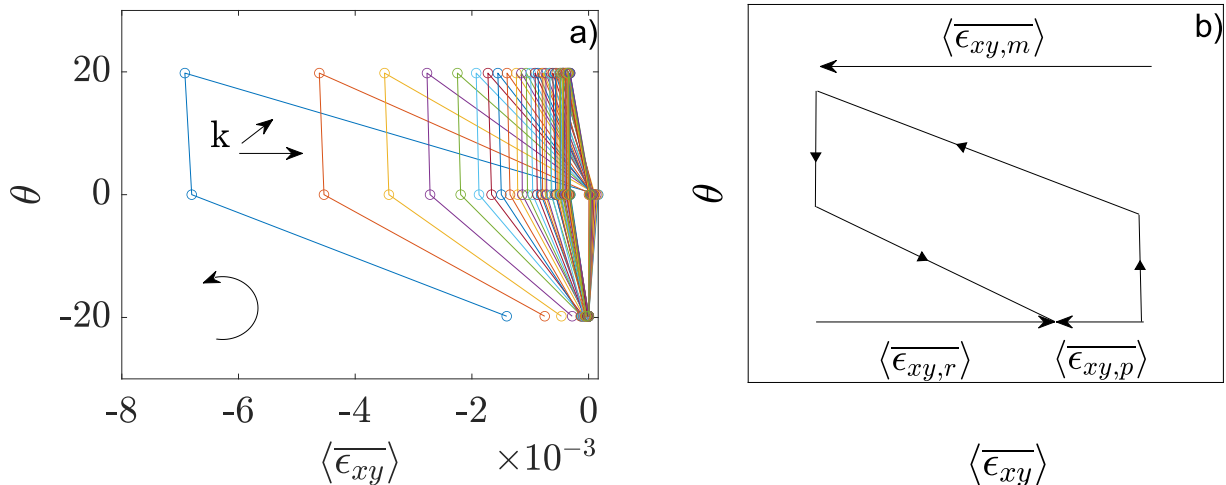


FIG. 4. a) Superposition of shear cycles at $\theta_m = 19.8^\circ$ (Position $P1$, $k_r = 3$). Cycles are in the anticlockwise direction, as indicated by the arrow. The first cycle (blue line) has the largest amplitude of deformation, and the following ones shift to the right. b) Sketch of a typical cycle with annotation of some intra-cycle strains as considered in the analysis (see text).

thickness $4d$, and compute the strain for each stripe. The profiles of volumetric strain between $[a_{k_r}, a_{50}]$ are shown in Figure 3 b) as a function of depth, along with an exponential fit of the form $\langle \overline{\epsilon_v} \rangle \propto \exp\left(-\frac{y}{y^*}\right)$. A similar profile is observed for each oscillation angle θ_m , with the characteristic cutoff length $y^* = 11.4 \pm 3$ mm.

B. Macroscopic strain cycles and local strain fluctuations

1. θ - ϵ cycles

In Figure 4a), we plot θ - ϵ cycles, focusing on the shear strain $\langle \overline{\epsilon_{xy}} \rangle$ at position $P1$ for $\theta_m = 19.8^\circ$. As the granular material compacts, the maximum intra-cycle shear strain $\langle \overline{\epsilon_{xy,m}} \rangle$, defined as the strain between $[c_k, a_{k+1}]$ and illustrated in Figure 4b), decreases with the number of oscillations. Additionally, between $[a_k, a_{k+1}]$, each cycle is characterized by finite plastic deformation $\langle \overline{\epsilon_{xy,p}} \rangle$ (see also Figure 4b). After a large number of oscillations, the cycles stabilize and the plastic strain disappears. This stabilization, along with permanent cumulative deformation, is referred to as "accommodation" in soil mechanics [27].

2. Strain heterogeneities.

An example of a deformation map for the interval $[a_{k_r}, a_{50}]$ is shown in Figure 5 a), where both volumetric and shear strains are presented. The strain distribution is spatially heterogeneous across two length scales. At the grain scale, adjacent Bagi cells can exhibit strain differences by several orders of magnitude, with strains that can even have opposite signs. At the larger scale represented by the characteristic cutoff length y^* in Figure 3 b), the strain map shows that that strain is more pronounced near the free surface.

In Figure 5 b), we present the strain and its root-mean-square fluctuation $\delta\epsilon_p = \left(\langle \overline{\epsilon_p^2} \rangle - \langle \overline{\epsilon_p} \rangle^2\right)^{1/2}$ for the interval $[a_{k_r}, a_k]$, which corresponds to the total plastic deformation accumulated during a given cycle. For both the shear and volumetric components, the root-mean-square fluctuations are approximately ten times greater than the mean, with $\delta\epsilon_p \approx \langle \overline{\epsilon_p^2} \rangle^{1/2} \gg |\langle \overline{\epsilon_p} \rangle|$. This is not attributable to the heterogeneity of the mean strain, as an exponential profile leads to a variability of the same order of magnitude as the mean. Furthermore, the fluctuations are not influenced by the reproducibility of $\langle \overline{\epsilon_p} \rangle$ across different experiments, as shown by the error bars in Figure 5 b), which are much smaller than the fluctuations themselves. Therefore, the fluctuations are primarily governed by the strain heterogeneity at the grain scale, caused by the erratic motions of the grains. These motions are the dominant source of decorrelation in the scattered waves, which is quantified by g_1 . From this point onward, we will refer to $\delta\epsilon \approx \langle \overline{\epsilon^2} \rangle^{1/2}$ as fluctuations

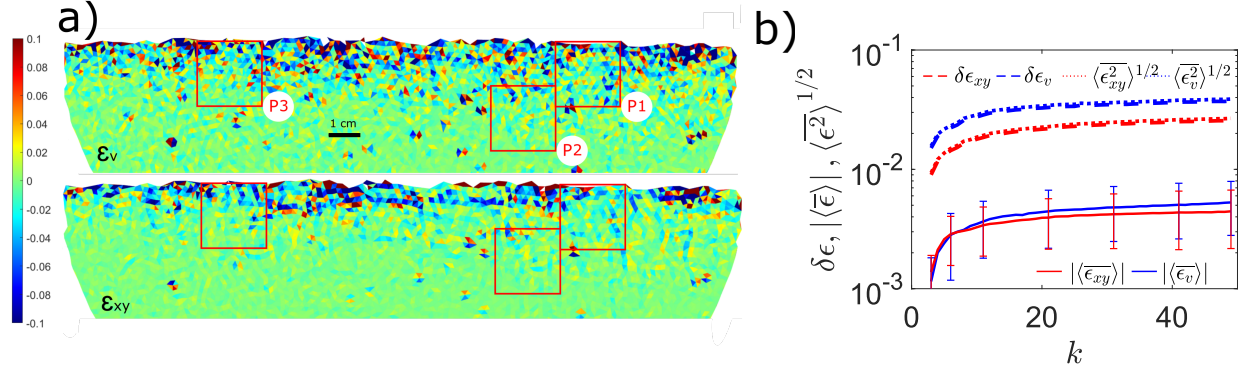


FIG. 5. a) Maps of Bagi cells for plastic volumetric strain (upper panel) and plastic shear strain (lower panel) for $\theta_m = 19.8^\circ$, pair $[a_{k_r}, a_{50}]$. The upper portion of each panel corresponds to the free surface. b) Plot of $|\langle \epsilon_v \rangle|$, $|\langle \epsilon_{xy} \rangle|$, $\langle \epsilon_v^2 \rangle^{1/2}$, $\langle \epsilon_{xy}^2 \rangle^{1/2}$, and $\delta \epsilon_v$, $\delta \epsilon_{xy}$ as a function of the number of oscillations k , at position $P1$ for $\theta_m = 19.8^\circ$. Data are presented for pairs $[a_{k_r}, a_k]$. The ordinate is shown on a logarithmic scale for convenient visualization of the data. The error bars on the $|\langle \epsilon_v \rangle|$ and $|\langle \epsilon_{xy} \rangle|$ curves represent the standard deviation arising from the variability in the mean deformation between different experiments (10 in total).

at the grain scale.

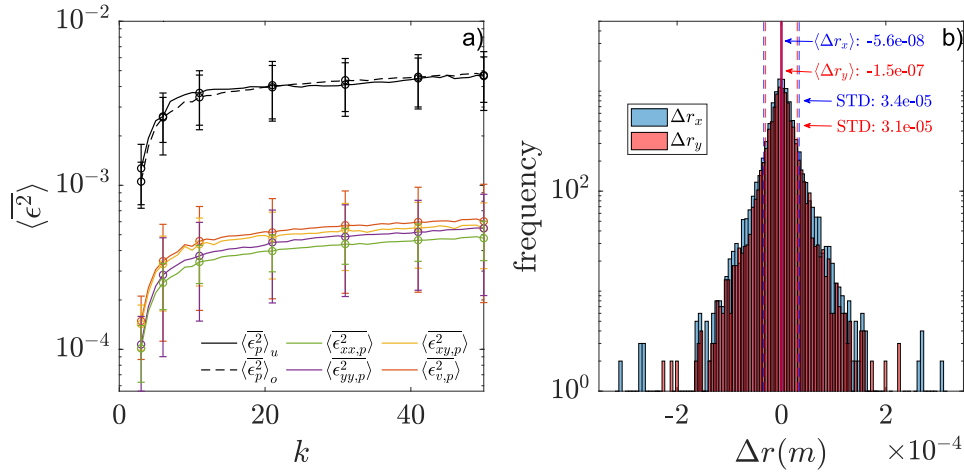


FIG. 6. a) Quadratic plastic strain components as a function of the number of oscillations. b) Distribution of the relative displacements $\langle \Delta r_x \rangle$ and $\langle \Delta r_y \rangle$ between cycles k_r and 50. In both panels a) and b), the data correspond to $\theta_m = 16.8^\circ$, position $P1$, and $k_r = 2$.

C. Quadratic terms from Bagi cells and DAWS

The quadratic strain terms obtained from the two methods are plotted in Figure 6 a) for the interval $[a_{k_r}, a_k]$ and $\theta_m = 16.8^\circ$ at position $P1$. The quantities $\langle \epsilon_{xx}^2 \rangle$, $\langle \epsilon_{yy}^2 \rangle$, $\langle \epsilon_{xy}^2 \rangle$, and $\langle \epsilon_v^2 \rangle$ in Bagi cells similarly increase with the number of oscillations and are all of the same order of magnitude. Their sum, $\langle \bar{\epsilon}^2 \rangle_o = \left(\langle \epsilon_v^2 \rangle + 2 \times \sum_{i,j} \langle \epsilon_{i,j}^2 \rangle \right)$ ($i, j \neq z$), can be compared to $\langle \bar{\epsilon}^2 \rangle_u$, which is derived from the inversion of Eq. 4 and includes all squared components of the strain tensor. Figure 6 a) shows that $\langle \bar{\epsilon}^2 \rangle_o$ and $\langle \bar{\epsilon}^2 \rangle_u$ are in good agreement. Therefore, comparing our experimental results with the theoretical predictions from [25] (Eq. 4), suggests that the quadratic terms $\langle \epsilon_{xz}^2 \rangle$, $\langle \epsilon_{yz}^2 \rangle$, and $\langle \epsilon_{zz}^2 \rangle$ can be neglected.

A comparison between both methods is also possible via the estimate of the root-mean-square relative displacements

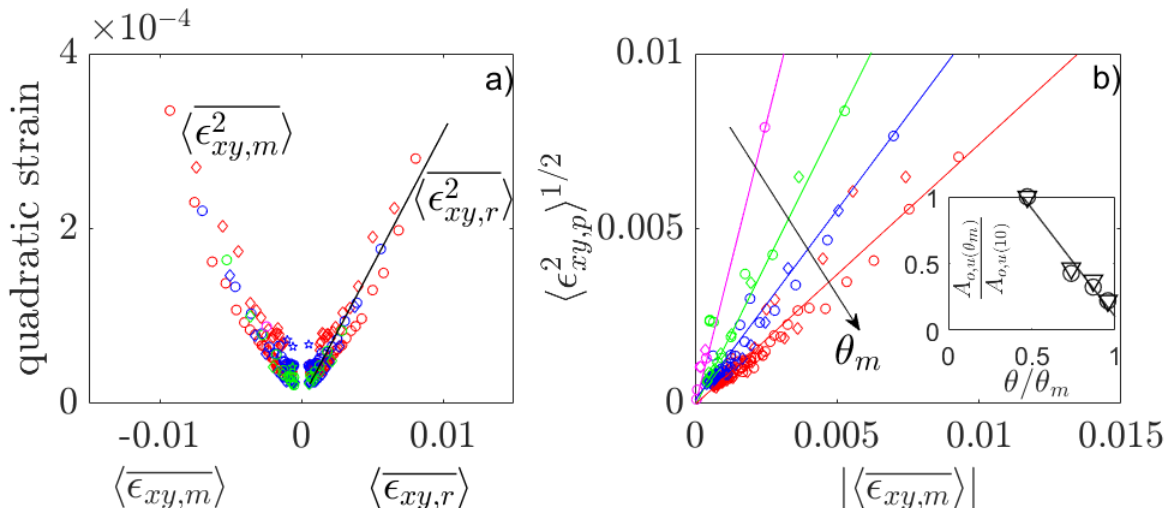


FIG. 7. a) Mean square strain from Bagi cells as a function of the average shear strain $\langle \overline{\epsilon_{xy,m}} \rangle$ and the average backward shear strain $\langle \overline{\epsilon_{xy,r}} \rangle$. b) Plastic strain fluctuations from Bagi cells as a function of the maximum strain $|\langle \overline{\epsilon_{xy,m}} \rangle|$. In panels a) and b), circles correspond to position $P1$, and diamonds to position $P3$. Position $P2$, represented by stars, is plotted only in panel a). The colors red, blue, green, and violet correspond to measurements at $\theta_m = 21.8^\circ$, 19.8° , 16.8° , and 10.8° , respectively. Inset of b): Circles represent $A_o(\theta_m)$ from Eq. 5 (Bagi cells), normalized by $A_o(10.8^\circ) = 3.3$. Triangles represent $A_u(\theta_m)/A_u(10.8^\circ)$ from DAWS (see Figure 11b in Appendix A), with $A_u(10.8^\circ) = 8.3$. The line is a linear fit to the data: $A_{o,u}(\theta_m)/A_{o,u}(10.8^\circ) = 1.6 \times (1 - \frac{\theta_m}{\theta_r})$.

between grains. From the imaging method, computing the relative displacement Δr between nearest neighbors yields the distributions Δr_x and Δr_y , as shown in Figure 6b). We find $\langle \overline{\Delta r_x^2} \rangle_o^{1/2} \approx 34 \mu\text{m}$ and $\langle \overline{\Delta r_y^2} \rangle_o^{1/2} \approx 31 \mu\text{m}$. Turning to DAWS, we calculate from Eq. 3 and 4 that in all cases $V(\Delta\Phi) \gg \langle \Delta\Phi \rangle^2$. Hence, $V(\Delta\Phi) \approx \langle \Delta\Phi^2 \rangle \sim q^2 \langle \Delta r^2 \rangle_u / 3$ [15]. From Figure 6a), we find that $\langle \overline{\epsilon^2} \rangle_u \sim 10^{-3}$, which leads to $\langle \overline{\Delta r^2} \rangle_u^{1/2} \sim 47 \mu\text{m}$, similar to the value obtained from the optical method. It is important to note that the relative mean squared displacement $\langle \Delta r^2 \rangle_u$ measured by multiply scattered waves does not depend on the symmetric strain tensor and is therefore distinct from the more commonly used mean square displacement derived from the displacement gradient tensor.

In summary, DAWS and the optical method based on Bagi cells provide consistent independent measurements of strain fluctuations. The optical method has the advantage of allowing the calculation of average deformation but is limited to the study of grains in contact with the solid walls. In contrast, DAWS captures the sum of all squared strain terms in the bulk but cannot measure the average strain.

D. Strain fluctuations : Intracycle diffusion and plasticity.

Since all measured quadratic strain terms are equivalent, and for the sake of conciseness, the remainder of the paper focuses on describing one specific strain component: the shear component (optical method). In particular, we emphasize how the shear strain $\epsilon_{xy,p}^2$ between $[a_k, a_{k+1}]$ is derived from the consecutive forward (maximum) strain $\epsilon_{xy,m}$ over the interval $[c_k, a_{k+1}]$ and the backward (return) strain $\epsilon_{xy,r}$ over $[a_k, c_k]$, as illustrated in Fig. 4b). Data from the optical method are presented in the main text, while complementary data from DAWS, leading to the same conclusions and suggesting that the observed effects are not confined to the possible peculiarities of grains at the solid walls, are reported in Appendix C.

The variation of the quadratic strain as a function of both $\langle \overline{\epsilon_{xy,m}} \rangle$ and $\langle \overline{\epsilon_{xy,r}} \rangle$ from Bagi cells is plotted in Figure 7a) for all three zones of interest and the four oscillation angles. All data collapse onto a single curve, which can be approximated linearly by $\langle \overline{\epsilon_{xy,r,m}^2} \rangle = D_o \times |\langle \overline{\epsilon_{xy,r,m}} \rangle|$, with $D_o \approx 0.025$. The data exhibit consistent "diffusive" behavior, driven by mechanical energy [28–30]. It is important to note that the term "diffusion" is used here to describe the proportionality between strain fluctuations and mean strain, as seen in athermal amorphous systems [30]. The plasticity observed at the end of an oscillation arises from two consecutive forward and backward diffusive branches.

The fluctuations of the plastic strain $\langle \overline{\epsilon_{xy,p}^2} \rangle^{1/2}$ from Bagi cells are plotted in Figure 7 b) as a function of $|\langle \overline{\epsilon_{xy,m}} \rangle|$ for zones of interest P1 and P3 and all the oscillations angles. Plastic quadratic terms from P2 are not discussed because the values are too close to the noise level $\sim 10^{-4}$. A first observation is that $\langle \overline{\epsilon_{xy,p}^2} \rangle^{1/2}$ has a linear dependence

on the mean strain, as opposed to the diffusive forward and backward strains above. Second, at fixed strain, higher oscillation angles give rise to lower fluctuations. This can be described by

$$\delta\epsilon_{xy,p} \approx \langle \epsilon_{xy,p}^2 \rangle^{1/2} = A_o |\langle \epsilon_{xy,m} \rangle| \quad (5)$$

A_o is a function of θ_m is plotted in Figure 7 b) (inset) showing a linear decrease. As shown in the Figure 11 of Appendix A we find similar behavior with DAWS. At this stage, our experimental data from two different methods show that (i) the strain is diffusive (ii) the fluctuations of the plastic strain vary linearly with the maximum shear strain and (iii) at fixed strain, fluctuations decrease with the oscillation angle.

IV. DISCUSSION

For the free-surface configuration used in the present study, the rotation of the system by an angle θ_m is equivalent to the application of a shear stress of the order $\sigma_m \sim \Delta\rho\phi h \sin\theta_m$, where $\Delta\rho = \rho_g - \rho_w$ (with ρ_g and ρ_w being the densities of the grains and water, respectively), $\phi = \phi(\theta_m, k)$ is the packing fraction, and $h = 13d$ is the size of the zones. According to the preparation protocol (Figure 1 a)), all samples exhibit the same global initial packing fraction $\phi_0 \approx 0.61$, which is obtained from the position of the free surface averaged over all experiments.

To estimate the packing fraction ϕ of the material located in the zones $P1$ and $P3$, we use the relation $\phi \approx \phi_0 (1 + \langle \bar{s}_y \rangle / h)$, where $\langle \bar{s}_y \rangle$ is the position of the free surface, as shown in Figure 3 a). The difference in packing fraction between two systems sheared at different θ_m values is given by $\Delta\phi/\phi_0 \approx \langle \bar{s}_y \rangle / h \ll \Delta\theta_m/\theta_m$. Moreover, at a fixed θ_m , the relative variation of packing fraction during compaction is small, on the order of $\sim 10^{-2}$. Therefore, θ_m determines the constant maximum stress applied at each cycle, independent of ϕ . However, the repeated oscillations at θ_m do modify the packing fraction by playing the role of mechanical taps, as discussed earlier.

We assume, as suggested by the shear cycles shown in Figure 4 a), a constitutive relation between ϵ_{xy} , θ , and ϕ , where $\epsilon_{xy}(\theta, \phi)$ is an increasing function of θ_m and a decreasing function of ϕ . Thus, Eq. 5 becomes $\delta\epsilon_{xy,p} = A_o(\theta_m) \times |\langle \epsilon_{xy,m} \rangle|(\theta_m, \phi)$. In combination with the second relation, $A_o(\theta_m) \propto \left(1 - \frac{\theta_m}{\theta_r}\right)$ from Figure 7 b) (inset), we can describe the data.

To do so, the fluctuations of the plastic strain are re-plotted in Figure 8 b) as a function of ϕ , estimated using the expression above (the following analysis is not sensitive to small variations of ϕ_0 and h , nor to the particular method used to calculate the packing fraction.) At fixed θ_m , the fluctuations of plastic strain grow with ϵ and correspond to a decrease in packing fraction. At fixed ϵ (iso-strain dashed lines in Figure 8 b)), the plastic strain fluctuations increase with decreasing θ_m via A_o , as observed in Figure 7 b). This in turn forces ϕ to decrease. Hence, we observe larger plastic fluctuations in looser systems both at fixed strain and at fixed stress. The case at fixed ϕ is more complex. Increasing θ_m increases the strain but decreases A_o . Comparison of iso- ϕ data at $\phi \sim 0.65$ in Figure 8 b) for $\theta_m = 19.8^\circ$ and 21.8° suggests that fluctuations increase with higher stress, and the stress-strain constitutive relation dominates over the moderate effect of θ_m on A_o .

Although the causality between the high fluctuations and the low packing fraction is not established, our results suggest that the free volume [31] could play a role in the emergence of plastic fluctuations. Following [31], an estimate of the average free volume per particle is $v_f = V_g \frac{\phi_c - \phi}{\phi_c^2}$ (where V_g is the volume of a grain and $\phi_c = 0.74$ is the close packing fraction), and assuming that v_f is homogeneously distributed around the particles, one can estimate a characteristic "free length", l_f , available for the particle to rearrange. For the conditions of Figure 6 b) (with $\phi \approx 0.64$), we obtain $l_f \approx 85 \mu\text{m}$, to be compared with the root-mean-square relative particle displacements $\langle \Delta r^2 \rangle_o^{1/2} \approx 30 \mu\text{m}$. The correspondence between the two orders of magnitude suggests that higher free volume provides more room for exploration of the topological landscape, leading to prominent chaotic irreversible relative displacements between the grains and higher fluctuations.

Lastly, we explain how the experimental relationship in Eq. 5 arises from the cumulative effect of two consecutive "diffusive" branches. To illustrate this, we propose a straightforward description of a strain cycle, where the total plastic strain at the end of the cycle is the sum of the forward strain, $\langle \epsilon_{xy,m} \rangle$, and the backward strain, $\langle \epsilon_{xy,r} \rangle$ (see Figure 4 b)). As shown earlier, the mean square of the strain exhibits diffusive behavior, described by $\langle \epsilon_{xy,m,r}^2 \rangle = D_o |\langle \epsilon_{xy,m,r} \rangle|$ where D_o is the diffusion coefficient. Treating the strain in the Bagi cell as a random variable, the total strain can be written as $\epsilon_p = \epsilon_m + \epsilon_r$. The variance of the total strain is then given by $V(\epsilon_p) = V(\epsilon_m) + V(\epsilon_r) + 2\text{cov}(\epsilon_m, \epsilon_r)$, where V represents the variance and cov is the covariance. We further assume that the forward and backward mean strains are related by a linear relationship $\langle \epsilon_{xy,r} \rangle = -b\langle \epsilon_{xy,m} \rangle$ where $b = b(\theta_m)$ and $0 \leq b \leq 1$. The parameter $b \rightarrow 1$ (or $b \rightarrow 0$) corresponds to a more elastic (or plastic) behavior. Consequently, the mean square of the plastic strain can be approximated as $\langle \epsilon_{xy,p}^2 \rangle \approx \alpha |\langle \epsilon_{xy,m} \rangle|$ where $\alpha = D_o(1 + b + 2b^{1/2}r_{mr})$ and r_{mr} is the correlation coefficient, defined as the covariance divided by the product of the standard deviations of the forward and backward strains, $\epsilon_{xy,m}$ and $\epsilon_{xy,r}$.

The parameters b and r_{mr} can be determined experimentally. Fitting the sum of the variances of forward and backward strains as a function of $\langle \overline{\epsilon_{xy,m}} \rangle$ yields the parameter $b \approx 0.5, 0.6, 0.7$ for $\theta_m = 16.8^\circ, 19.8^\circ$ and 21.8° , respectively (not shown). Moreover, r_{mr} , which is plotted in Figure 8 a), is negative (indicating anticorrelation between maximum and backward shear) and varies linearly with the strain $r_{mr} = c|\langle \overline{\epsilon_{xy,m}} \rangle| - 1$. The slope $c = c(\theta_m)$, given in Figure 8 a), is a decreasing function. Arranging the various terms above gives $\alpha = D_o(A_1 + A_2 \times |\langle \overline{\epsilon_{xy,m}} \rangle|)$ with $A_1 = (1 + b - 2b^{1/2})$ and $A_2 = 2b^{1/2}c$. α rationalizes our experimental findings in describing how diffusion, reversibility, and strain correlation couple to define plastic strain fluctuations.

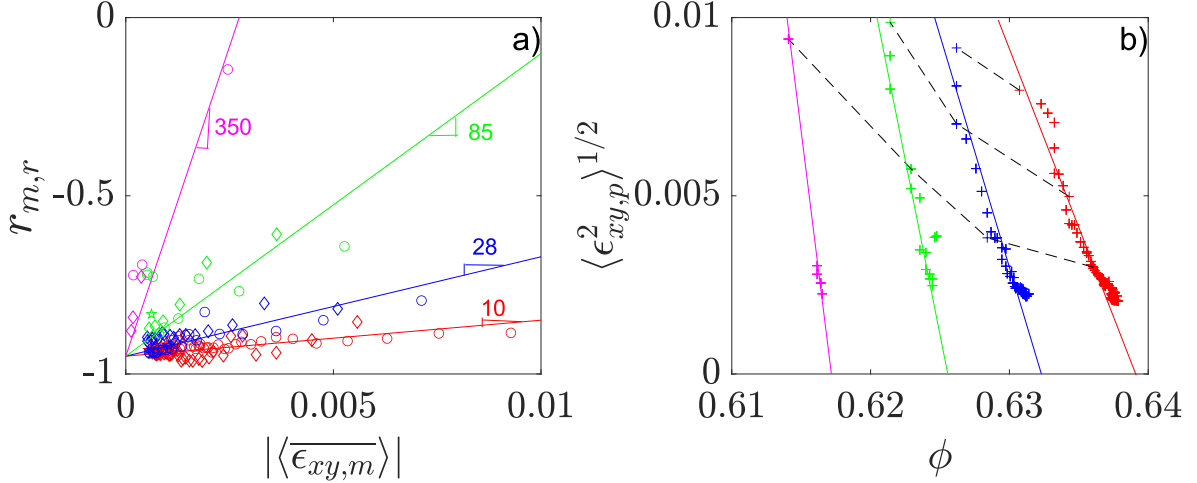


FIG. 8. a) Correlation between $\epsilon_{xy,m}$ and $\epsilon_{xy,r}$ strains in a shear cycle, with the slope c indicated next to the linear fit of the data for each angle. Red, blue, green, and pink lines and points correspond to $\theta_m = 21.8^\circ, 19.8^\circ, 16.8^\circ$ and 10.8° , respectively. b) Fluctuations of plastic strain as a function of the density of the packing estimated from the compaction near the free surface (see text). The crosses are the experimental points smoothed with a moving average of 4 points. Dashed lines represent iso-strain points, from bottom to top $\langle \overline{\epsilon_{xy,m}} \rangle = 2.5 \times 10^{-3}, 5.2 \times 10^{-3}, 6.9 \times 10^{-3}$. Plain lines are guides to the eye. The color code is the same as in a).

With the expression for α above, fluctuations vanish as expected for $\epsilon \rightarrow 0$. However, for larger strains ($> 10^{-3}$), the A_2 term dominates, and $\delta\epsilon_{xy,p} \sim (D_o A_2)^{1/2} |\langle \overline{\epsilon_{xy,m}} \rangle|$, which allows us to identify in Eq. 5 that $A_o = b^{1/4} (2cD_o)^{1/2}$. In our experiments, D_o is constant, and $b^{1/4}$ varies slowly, so A_o is primarily controlled by the parameter c . As a consistency check, A_o is plotted as a function of $c^{1/2}$ in Figure 12 in the Appendix D. The linear fit $A_o = 0.17 \times c^{1/2}$ is in good agreement with the independent estimate $b^{1/4} (2D_o)^{1/2} \approx 0.2$. This identifies the different physical mechanisms that govern the empirical parameter A_o . Diffusion, due to frictional and hard-sphere interactions, enhances plastic strain fluctuations. However, these fluctuations are moderated by the high local strain anticorrelation in dense packings, which we tentatively attribute to more reversible trajectories, associated to the memory effect.

To sum up, we find that the fluctuations of plastic strain are higher in the loosest packings, where the independence of forward and backward strains in Bagi cells is enhanced. Plasticity, viewed through the lens of local fluctuations, shares some common features but also exhibits differences with other divided systems such as emulsions and colloidal glasses. As in emulsions [10], fluctuations increase with decreasing packing fraction at fixed strain. However, in colloidal glasses [11], low packing fraction leads to fewer plastic events, as the lubricated interactions between grains allow for reversibility. Our study suggests distinct signatures of emerging plasticity in emulsions, colloidal glasses, and granular materials, shedding light on the effects of particle interactions.

V. CONCLUSION

We have experimentally studied, using a setup combining optical analysis and DAWs, the fluctuations of strain in a granular medium subjected to oscillatory stress. A detailed analysis of the sources of variability suggests that the strain fluctuations are governed by the local scale, which dominates the effect of the strain gradient along the vertical. Both methods provide similar results, allowing us to propose that the observations made by measuring the strain fluctuations through imaging the grains at the wall are relevant in the bulk. We find that the variance of the local strain is proportional to its mean, as seen in other amorphous systems. Furthermore, the fluctuations of plastic

strain arise from the interplay between diffusion and strain anticorrelation, with the latter being more pronounced in dense packings, thereby limiting erratic rearrangements due to the reduced free volume.

Acknowledgements

We thank D. Hautemayou, C. Mézière and P. Moucheront for their help in building the experimental setup. This work was funded by Labex MMCD.

-
- [1] A.S. Argon and H.Y. Kuo. *Materials Science and Engineering*, 39:101, 1979.
 - [2] D. Chen, K.W. Desmond, and E.R. Weeks. *Soft Matter*, 8:10486, 2012.
 - [3] K.E. Jensen, D.A. Weitz, and F. Spaepen. *Phys. Rev. E.*, 90:042305, 2014.
 - [4] G. Combe, V. Richefeu, M. Stasiak, and A. Atman. *Phys. Rev. Lett.*, 115:238301, 2015.
 - [5] F. Radjai and S. Roux. *Phys. Rev. Lett.*, 89:064302, 2002.
 - [6] Y. Cao et al. *Nat. Commun.*, 9:2911, 2018.
 - [7] O. Pouliquen, M. Belzons, and M. Nicolas. *Phys. Rev. Lett.*, 91:014301, 2003.
 - [8] C. Zhai, N. Albayrak, J. Engvist, S. Hall, J. Wright, M. Majkut, E.B. Herbolz, and R.C. Hurley. *Phys. Rev. E*, 105:014904, 2022.
 - [9] R. Höhler, S. Cohen-Addad, and H. Hoballah. *Phys. Rev. Lett.*, 79:1154, 1997.
 - [10] P. Hébraud, F. Lequeux, J.P. Munch, and D.J. Pine. *Phys. Rev. Lett.*, 78:4657, 1997.
 - [11] G. Petekidis, A. Moussaïd, and A.N. Pusey. *Phys. Rev. E*, 66:051402, 2002.
 - [12] A. Amon, V. Bau Nguyen, A. Bruand, J. Crassous, and E. Clément. *Phys. Rev. Lett.*, 108:135502, 2012.
 - [13] A. Le Bouil, A. Amon, S. McNamara, and J. Crassous. *Phys. Rev. Lett.*, 112:246001, 2014.
 - [14] N. Menon, , and D.J. Durian. *Science*, 275:1920, 1997.
 - [15] M.L. Cowan, I.P. Jones, J.H. Page, and D. A. Weitz. *Phys. Rev. E*, 65:066605, 2002.
 - [16] J. Léopoldès and X. Jia. *Soft Matter*, 16:10716, 2020.
 - [17] W.E.H. Culling. *J. Geol.*, 71:127, 1963.
 - [18] J. Choi, A. Kudrolli, R.R. Rosales, and M.Z. Bazant. *Phys. Rev. Lett.*, 92:174301, 2004.
 - [19] H.M. Jaeger, C. Liu, and S.R. Nagel. *Phys. Rev. Lett*, 62:266001, 1989.
 - [20] Uwe Schmidt, Martin Weigert, Coleman Broaddus, and Gene Myers. Cell detection with star-convex polygons. *CoRR*, abs/1806.03535, 2018.
 - [21] J.C. Crocker and D.G. Grier. *J. Colloid Interface Sci.*, 179:298, 1996.
 - [22] K. Bagi. *Mechanics of Materials*, 22:165, 1996.
 - [23] S.B. Savage and R. Dai. *Mechanics of materials*, 16:225, 1993.
 - [24] P. Sheng. *Introduction to Wave Scattering, Localization and Mesoscopic Phenomena*. Springer, 2006.
 - [25] D. Bicout and R. Maynard. *Physica A*, 199:387, 1993.
 - [26] E.R. Nowak, J.B. Knight, E. Ben-Naim, H.M. Jaeger, and S. R. Nagel. *Phys. Rev. E.*, 57:1971, 1998.
 - [27] Bernard Cambou and Pierre-Yves Hicher. *Elastoplastic Modeling of Soils: Cyclic Loading*, chapter 4, pages 143–186. John Wiley and Sons, Ltd, 2008.
 - [28] B. Utter and R.P. Berhinger. *Phys. Rev. E*, 69:031308, 2004.
 - [29] D.M. Mueth. *Phys. Rev. E.*, 67:011304, 2003.
 - [30] C.E. Maloney and M.O. Robbins. *J. Phys. Condens. Matter*, 20:244128, 2008.
 - [31] T. Boutreux and P.G. de Gennes. *Physica A*, 244:59, 1997.
 - [32] H.K. Kytömaa. *Powder Technology*, 82:115, 1995.

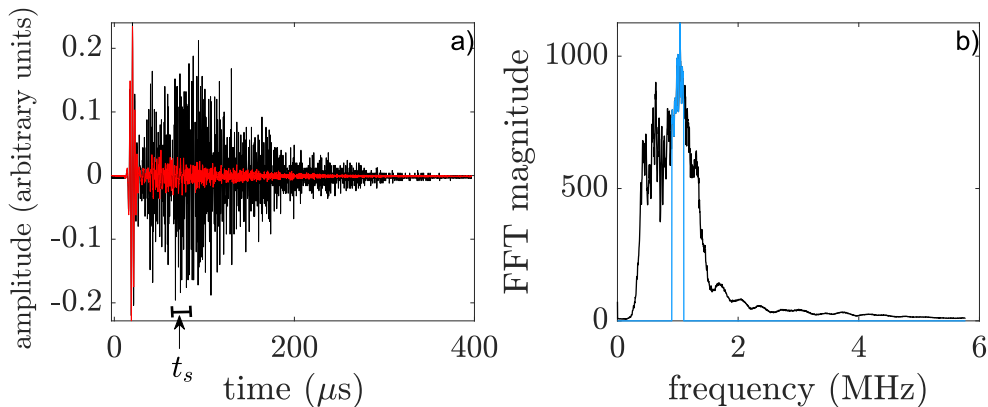


FIG. 9. (a) The black curve represents a typical signal transmitted through the granular suspension, while the red curve corresponds to the coherent part, obtained by averaging 10^2 signals from different packings after multiple full rotations of the drum. The window used to compute the signal decorrelation is taken at t_s (see text). (b) Average spectrum of the transmitted signal, with the filtering window (in cyan) centered at $1 \text{ MHz} \pm 10\%$.

Appendix A: DAWS

With an appropriate rotation of the drum, the emission-reception transducers can be positioned such that their axis passes through the center of the study areas ($P1$, $P2$, or $P3$ in Figure 2 a)). The recorded signals consist of a coherent component, while the scattering effects are captured in the late "coda" part, as illustrated in Figure 9 a). The coherent part (red signal in Figure 9 a)) is obtained by averaging one hundred signals transmitted through independent configurations, each acquired after several full rotations of the drum. This coherent wave is subtracted from raw signals, which are subsequently filtered to $1 \text{ MHz} \pm 10\%$ (see Figure 9 b)).

When the drum oscillates below the angle of repose, the relative motion of the grains induces changes in the ultrasound signals. The coherent part of the signal depends on the average properties of the medium, such as the effective bulk modulus and density.

For the calculation of correlations between signals, we select a window between $65 \mu\text{s}$ and $85 \mu\text{s}$, centered around the propagation time t_s , which corresponds to the maximum of the transmitted intensity (see Figure 9 a)), as obtained from the envelope of 10^2 signals from different configurations. This time can be interpreted as the time required for scattered waves to probe a volume of the order of L^3 , where L is the thickness of the drum. Indeed, scattered waves explore a typical length scale diffusively, given by $\sqrt{6\mathcal{D}t}$, where \mathcal{D} is the diffusion coefficient of the waves. With an order of magnitude estimate $\mathcal{D} \sim 1 \text{ mm}^2/\mu\text{s}$ [15] and $L = 20 \text{ mm}$, we obtain a typical timescale $t_D \sim 70 \mu\text{s}$, comparable to t_s . The number of scattering events along the acoustic path is estimated as $n \sim t_s v_e / l$, where t_s is the time associated with the chosen temporal window, and v_e is the energy velocity. Assuming $v_e \approx v$, the sound speed in water, and $\lambda \approx l$, $n \sim t_s f = 80$ (f is the frequency).

Unlike previous studies in the incompressible limit [15], the oscillations of the drum in our experiment induce compaction in the granular medium. This compaction has a small yet significant effect on the \cos term in Eq. 2, requiring a correction of approximately 10% to g_1 for accurate calculation of the phase variance. Using the model proposed by [32], we have verified that the volumetric strain estimated from variations in the time of flight (coherent component of the acoustic signals) is consistent with values obtained through grain tracking (Bagi cells). The correction to g_1 based on volumetric strain can be applied using either of these two measurements.

Appendix B: Fitting parameters for the global compaction

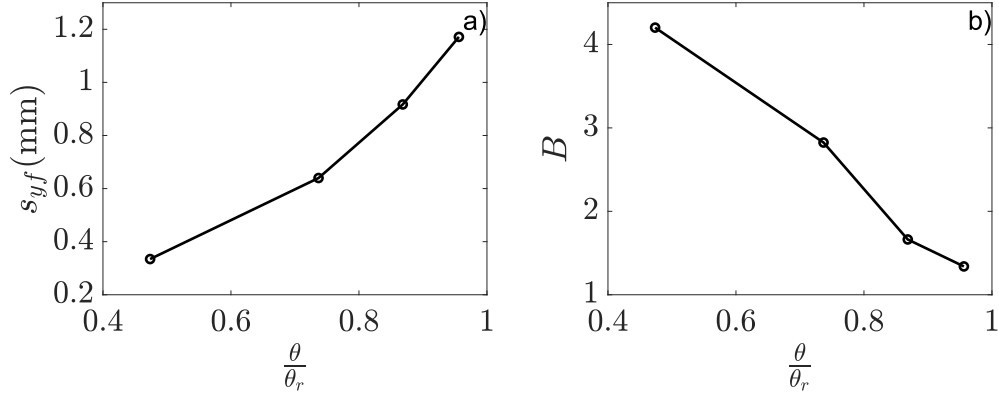


FIG. 10. Parameters obtained from fitting, with Equation B1, the displacement of the free surface during compaction at different oscillation angles θ_m . The oscillation angle is normalized by the angle of repose θ_r .

For the material located between the free surface and of height h the global packing fraction ϕ , which represents a measure of the compaction fraction, is related to the volumetric strain ϵ_v , by :

$$\epsilon_v = \frac{\Delta V}{V_0} = -\frac{\Delta\phi}{\phi_0} \sim -\frac{s_y}{h},$$

with V_0 , ϕ_0 the volume and the packing density of the reference packing. s_y is the displacement of the free surface. This amounts to

$$\phi = \frac{\phi_0(s_y + h)}{h}.$$

With the expression in [26] :

$$\phi = \phi_f - \frac{\phi_f - \phi_0}{1 + B \ln\left(1 + \frac{t}{\tau}\right)},$$

we obtain :

$$s_y = s_{yf} - \frac{s_{yf}}{1 + B \log(1 + k)}, \quad (\text{B1})$$

This equation was used to fit our experimental data describing the displacement of the free surface during the compaction oscillations. The variable s_y represents the position of the surface during the compaction cycle k , while s_{yf} corresponds to the final position of the surface after 50 cycles of compaction, reflecting the most compact state reached during the process.

Higher values of s_{yf} indicate more densely compacted systems at the end of the compaction cycles, as inferred from the final position of the free surface. The dimensionless parameter B characterizes the kinetics of compaction, where lower values of B correspond to faster compaction dynamics.

Appendix C: Quadratic strain from DAWS

In Figure 11 a), the sums of the quadratic terms obtained from DAWS (three positions, four angles) are plotted as a function of the mean strain measured in Bagi cells in the same conditions. We obtain $\langle \epsilon^2 \rangle_u = D_u \times |\langle \epsilon_{xy,r,m} \rangle|$ with $D_u \approx 0.17$. The ratio $D_o/D_u \sim 10^{-1}$ is as expected, confirming the agreement between the quadratic terms from the optical method and DAWS.

With DAWS, we also found a linear relation $\langle \epsilon_p^2 \rangle_u^{1/2} = A_u |\langle \epsilon_{xy,m} \rangle|$ as shown in Figure 11 b). For better comparison, $A_u = A_u(\theta_m)$ is plotted together with A_o in the inset of Figure 7 b) (main text), and has a similar dependency on the oscillation angle. Both methods show that, at fixed strain, the fluctuations of plastic strain decrease linearly with θ_m .

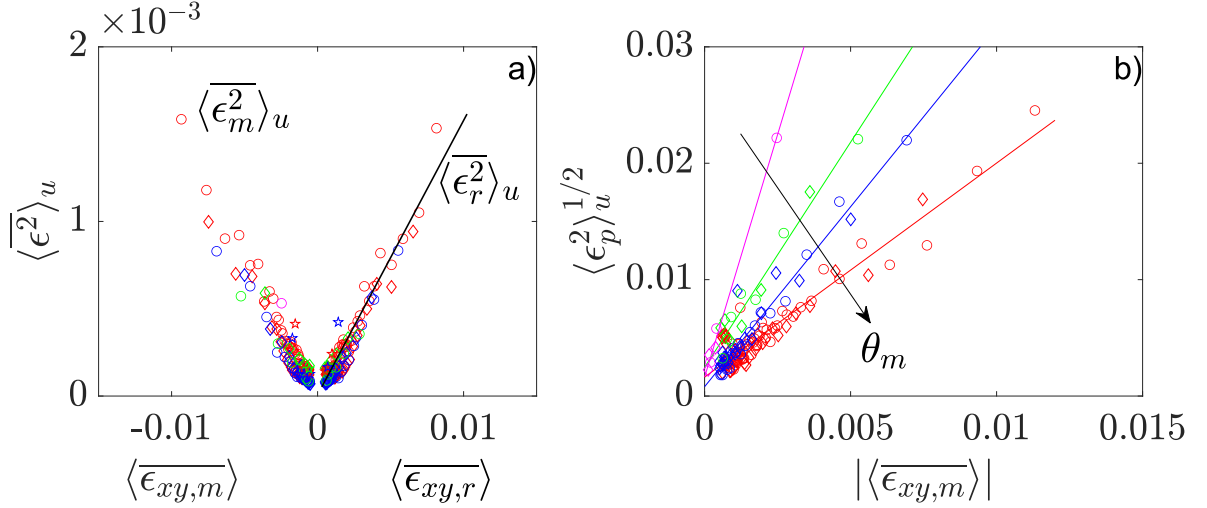


FIG. 11. a) Mean square strain from DAWS plotted versus the average shear strain $\langle \epsilon_{xy,m} \rangle$ and average backward shear strain $\langle \epsilon_{xy,r} \rangle$, corresponding to pairs $[a_k, c_k]$ and $[c_k, a_{k+1}]$, respectively. b) Fluctuations of plastic strain from DAWS as a function of maximum strain $|\langle \epsilon_{xy,m} \rangle|$. Circles: position $P1$. Losange: position $P3$. Stars: position $P2$. Red, blue, green and violet represent measurements at $\theta_m = 21.8^\circ, 19.8^\circ, 16.8^\circ$ and 10.8° respectively. In b), only positions $P1$ and $P3$ are represented. For a) and b), the values of $\langle \epsilon_{xy,m} \rangle$ and $\langle \epsilon_{xy,r} \rangle$ used for building the abscissa are the same as in Figure 7 a) and b), and determined from optics.

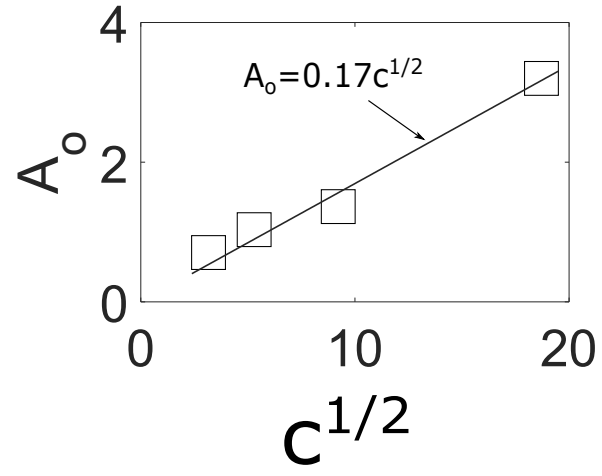
Appendix D: Linearity between parameters c and A_o 

FIG. 12. Parameter A_o plotted versus $c^{1/2}$. Squares: experimental data. The plain line is a linear fit to the data.